Journal of Medical Systems (2019) 43: 310
https://doi.org/10.1007/s10916-019-1433-z

IMAGE & SIGNAL PROCESSING

Multiscale Time-Sharing Elastography Algorithms and Transfer Learning of Clinicopathological Features of Uterine Cervical Cancer for Medical Intelligent Computing System

Xiaojun Dong[1] · Hongmei Du[2] · Haichen Guan[1] · Xuezhen Zhang[2]

Received: 5 May 2019 / Accepted: 7 August 2019 / Published online: 26 August 2019

Abstract
Intelligent medical diagnosis and computing system faces many challenges in complex object recognition, large-scale data imaging and real-time diagnosis, such as poor real-time computing, low efficiency of data storage and low recognition rate of lesions. In order to solve the above problems, this paper proposes a medical intelligent computing system and a series of algorithms for the clinical pathology of cervical cancer based on the multi-scale imaging and transfer learning framework. Firstly, based on data dimensions, imaging errors and other factors, this paper designs a multi-scale time-sharing elastic imaging algorithm based on image reconstruction time and data sample characteristics. Then, taking the burst imaging cohort and the calculation data set of new cervical cancer cases as the objects, based on the difficulties of cervical cancer feature modeling, this paper proposes the transfer learning algorithm of clinical and pathological features of cervical cancer. Finally, a medical intelligent computing system for cervical cancer pathology analysis and calculation with high efficiency and reliability is established. A series of proposed algorithms are compared with single-scale Retinex (SSR), which is based on single-scale Retinex migration learning (SSR-TL). The experimental results show that the proposed algorithm in cervical cancer pathological imaging and scoring, as well as the feature extraction and recognition of lesions, especially the efficiency of system execution, is obviously due to the comparison algorithm.

Keywords Time-sharing · Multiscale · Multiscale · Transfer learning · Medical intelligent computing

Introduction

Cervical cancer [1] and breast cancer [2] are two common malignancies in women. Among them, malignant tumors [3] occurring in the cervix and vagina and the cervical duct epithelium, namely cervical cancer, have different manifestations of the difficulty of lesion recognition and tumor diagnosis in different age groups, clinical manifestations and classification [4]. Imaging examination of cervical cancer plays a key role in the application of ultrasound, CT and MRI in clinical imaging and calculation. However, there are many challenges at present, such as the differentiated morphology [5] of cervical cancer lesions, uncertain boundaries [6], unknown internal echoes [7] and large-scale sample training.

About Imaging algorithm, article [8] presented a range migration algorithm for the multi-receiver synthetic aperture sonar based on Loffeld's bistatic formula, which consists of the quasi monostatic term, etc. The imaging algorithm proposed in article [9] combined the Barker coded excitation using the linear frequency modulated carrier with the synthetic aperture beam forming. Article [10] developed an imaging method for compensating the dispersion induced by the propagation distance. Article [11] proposed a parameter-free intravoxel incoherent motion imaging algorithm for assessment of cervical cancer. The image processing problem in article [12] can be performed over small-scale overlapping patches and be efficiently solved in a parallel or distributed manner.

About characteristic transfer learning, the authors of article [13] presented the application of deep learning combined with Transfer Learning for glitch classification, using real data from LIGO's first discovery campaign labeled by Gravity Spy, showing that knowledge from pre-trained models for real-world object recognition can be transferred for classifying

This article is part of the Topical Collection on *Image & Signal Processing*

✉ Xiaojun Dong
dongxj@students.solano.edu

[1] Hunan University of Medicine, Huaihua 418000, China

[2] The First People's Hospital of Huaihua, City, Huaihua 418000, China

spectrograms of glitches. The authors [14] argued that learning the latent attributes jointly with user-defined semantic attributes not only leads to better representation but also helps semantic attribute prediction. The authors [15] used the deep convolutional neural networks to identify the plant species captured in a photograph and evaluate different factors affecting the performance of these networks. The article [16] systematically investigated the process of transferring a Convolutional Neural Network, trained on ImageNet images to perform image classification, to kidney detection problem in ultrasound images. A regularization-based transfer learning strategy was proposed in article [17] that encourages source and target models to share the same coefficient sign.

About intelligent computing system, the study of knowledge-based systems and intelligent computing systems is presented in article [18], showing the methods and its salient features, processes and application areas in medical domain. A fuzzy k-nearest neighbor is used in article [19] to diagnose the possibly infected users, and Google map web service is used to provide the geographic positioning system-based risk assessment to prevent the outbreak. A computer-aided diagnosis system was proposed by using artificial intelligence for the diagnosis and characterization of thyroid nodules on ultrasound [20]. A novel self-organizing neural fuzzy inference system was developed in article [21] that functions as a reliable decision support system for ovarian cancer diagnoses.

However, the above research has not done detailed research on the feature modeling and feature extraction of cervical cancer and computing system. Based on the above results, the medical intelligent computing system is proposed by optimization and design of multiscale time-sharing elastography and Transfer learning of clinicopathological features algorithms.

The rest of this paper is organized as follows. Section "Multi-scale time-sharing elastic imaging algorithm" develops the Multi-scale time-sharing elastic imaging algorithm. Section "Transfer learning algorithm for clinicopathological features of cervical cancer" shows the Transfer learning algorithm for clinicopathological features of cervical cancer. Section "Medical intelligent computing system for clinical pathology of cervical cancer" indicates the Medical Intelligent Computing System for Clinical Pathology of Cervical Cancer. Section "System performance verification" perform the System performance verification, followed by the conclusion in Section "Conclusions".

Multi-scale time-sharing elastic imaging algorithm

The existing medical imaging algorithms and systems mainly have the following problems: 1. The imaging errors of high-dimensional data are large; 2. The reconstruction time of high-resolution images is long and the feature extraction of data samples is demanding; 3. The formation of long queues for large-scale BURST imaging tasks leads to the establishment of imaging data sets for a long time and the inefficiency of system execution; 4. The imaging method of multi-dimensional data dictionary. The time complexity is high and it requires many times of image reconstruction calculation. In order to solve these problems, we have established an efficient and reliable imaging mechanism based on the combination of multi-scale model and time-sharing elasticity.

Firstly, Fig. 1 illustrates the finite source imaging projection process for any high-dimensional sample set. In this arbitrary imaging region, the superposition of arbitrary high-dimensional data samples and finite element projection imaging meshes leads to the increase of imaging errors. Correspondingly, it is more difficult to extract data features based on the imaging projection formed by finite element method. The triangle in Fig. 1 represents the finite element. The dotted circle, the dotted rectangle and the solid ellipse represent the data sample space of different dimensions respectively. The matching relationship between the finite element method and the mapping is established according to the dimension difference and the image weight. In actual imaging, the location of imaging targets in different dimensions is unknown, so we design a multi-scale finite source imaging framework as shown in Fig. 2. In this framework, the finite element is mapped to multi-scale segmentation threshold, and the high latitude data is mapped to multi-scale stratification. In order to fully describe the real-time characteristics of random data samples in medical imaging area and accurately capture the data set, the multi-scale framework is based on the jitter of grid topology at any location. These jitters represent the real-time imaging characteristics of data sources and multi-dimensional samples in the whole high-dimensional imaging region. In order to count these jitters, the imaging responses of different dimensions and multi-scales in random imaging area were recorded, and the image weights of sample separation between scales were analyzed.

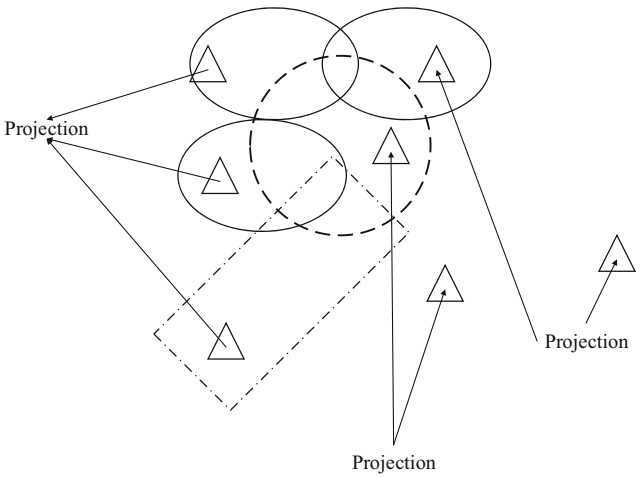

Fig. 1 Arbitrary high-dimensional imaging

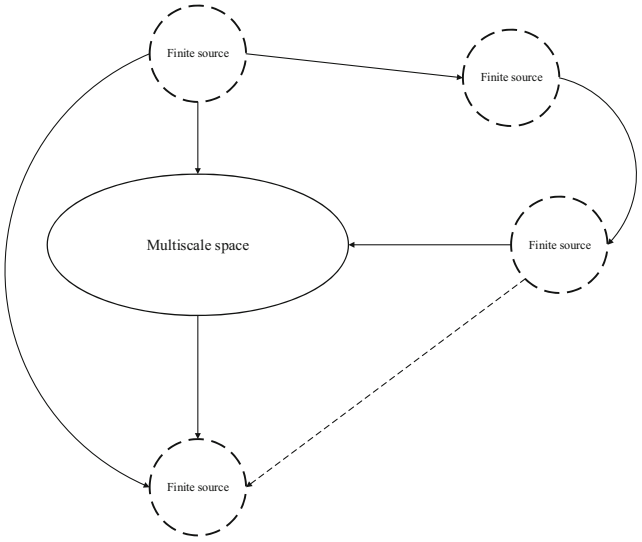

Fig. 2 Multi-scale finite source imaging

The scale of finite element data and low-dimensional multi-scale are related to high-dimensional multi-scale. The smaller the scale separation is, the smaller the scale of finite element data is, and the faster the convergence of low-dimensional multi-scale imaging iteration is. The larger the scale separation is, the larger the scale of finite element data is, and the faster the iteration convergence of high-dimensional multi-scale imaging is. Therefore, scale analysis S_A and finite metadata S_I can be estimated by the following formula.

$$\begin{cases} S_A = \dfrac{d^2}{\sqrt{\delta \sin\alpha}} \int_x f^2(x)dx \\ S_I = \dfrac{d^2}{\sqrt{\delta \sin\alpha}} \sum\limits_x \dfrac{f^2(x)}{1+E(S_A)} \end{cases} \tag{1}$$

Here, d is the Euclidean distance between the intense data cores of different scales shown in Fig. 2. δ denotes the dimensions at different scales for imaging data sets. Function f () is the projection of image data sample x, whose definition is determined by historical data sets and imaging parameters. The parameter α represent the angle between the data sample and the imaging projection. $E(S_A)$represents the expected value of scale analysis. The size of the expected value and its pain are very important for imaging. Rational selection of S_A and S_I is very important for the selection of imaging area and the preprocessing of sample set.

Based on the fusion of Figs. 1 and 2, we present a multi-scale imaging finite element processing flow, which is detailed in Fig. 3. The three core processes are represented by formulas 2, 3 and 4, respectively.

$$S_S = \int\limits_{d(x)} \frac{dx}{x}\left[S_A(f,\alpha) - \frac{\partial S_A(f,\alpha)}{\partial \alpha}\right] \tag{2}$$

Among them, S_S denotes the imaging scale of the superimposed region is represented. Function d(x) denotes

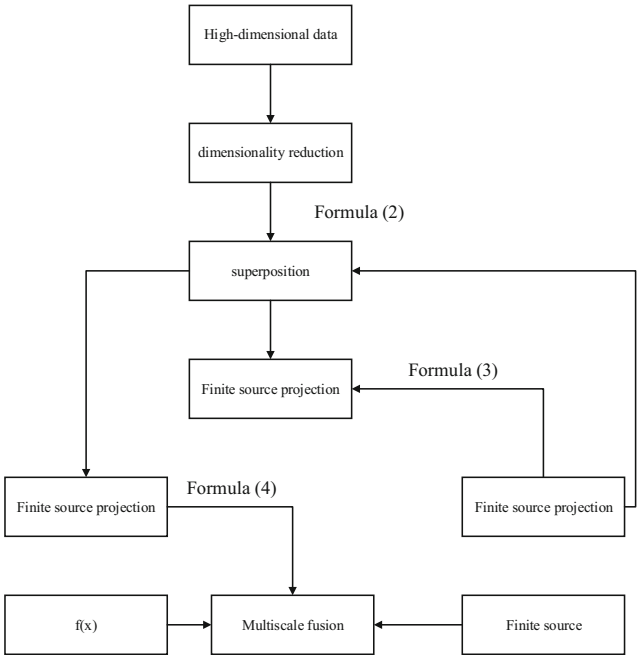

Fig. 3 Limited Source Processing Flow for Multiscale Imaging

the spacing of data sample x. The S_A in formula (1) is reconstructed into a function $S_A(f, \alpha)$.

$$P_{FS} = \begin{bmatrix} M_{(1,1)} & \cdots & \cdots & M_{(|P|,|FS|)} \\ \vdots & M_{(2,2)} & & \vdots \\ \vdots & & M_{(i,i)} & \vdots \\ M_{(|P|,|FS|)} & \cdots & \cdots & M_{(|P|,|FS|)} \end{bmatrix} \tag{3}$$

The matrix P_{FS} contains $|P| * |FS|$ elements. $M_{(|P|,|FS|)}$ can be obtained by formula (5).

$$g(M_S) = \begin{cases} \sum\limits_i \dfrac{[f(x_i)S_A]\sin\alpha}{\delta E(S_I)}, |FS| \geq E(S_I)\, E(S_I) \sum\limits_i [f(x_i)S_A] \dfrac{\sin\alpha}{\delta}, |FS| < E(S_I) \end{cases} \tag{4}$$

According to the limited source size and mapping accuracy, we define a function g (M_S) to represent the multi-scale fusion space region.

$$M_{(|P|,|FS|)} = \begin{cases} \left(\sum\limits_{i=1}^{|P|} |f\left(x_i^{|FS|}\right) - f\left(x_{\frac{|FS|}{|P|}}^{|FS|}\right)| \right), |P| \geq |FS| \\ \left(\sum\limits_{i=1}^{|FS|} |f\left(x_i^{|P|}\right) - f\left(x_{\frac{|P|}{|FS|}}^{|P|}\right)| \right), |P| < |FS| \end{cases} \tag{5}$$

Formula (4) shows that the performance of the above multi-scale fusion algorithm will continue to decline in the case of large-scale burst imaging. The main reason is that it cannot meet the need of parallel imaging. Therefore, we design a time-sharing multi-scale algorithm.

Based on the multi-scale fusion mechanism as shown in Fig. 3, we design the time-sharing multi-scale imaging architecture (see Fig. 4). we denote the vertical incidence of the

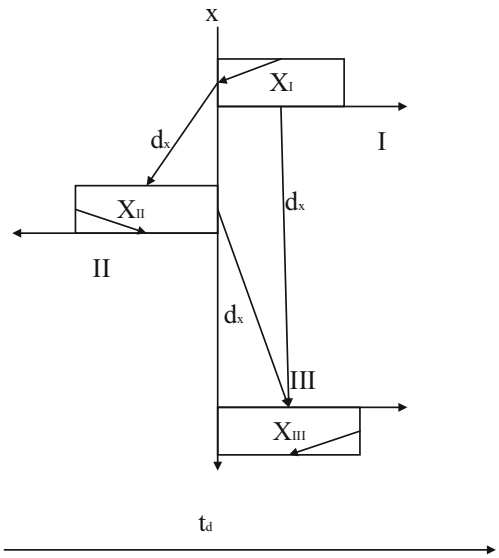

Fig. 4 Time-sharing multiscale imaging

multi-scale imaging data domain into the three-time layers as I, II and III respectively. Here, time layer I and II are the data sample space with the smallest scale difference. The discrete time point scale of time layer III is t_d. The time dispersion of each layer can be obtained by formula (6).

Multi-scale imaging of data set X_I in the first-time layer is $M_{(|X_I|,|FS|)}$. The multi-scale imaging of data set X_{II} in the second time layer is$M_{(|X_{II}|,|FS|)}$. Multi-scale imaging of dataset X_{III} in the third time layer is$M_{(|X_{III}|,|FS|)}$.

$$t_d = \begin{cases} \sum_{i=1}^{|X_I|} Y_i + \exp(-2\delta d(x)), x \in X_I \\ \dfrac{|P| \sum_{i=1}^{|X_{II}|} Y_i}{\exp(-2\delta d(x))}, x \in X_{II} \\ \dfrac{\sqrt{|FS| \sum_{i=1}^{|X_{III}|} Y_i}}{\exp(-2\delta d(x))}, x \in X_{III} \end{cases} \tag{6}$$

However, time-sharing multi-scale medical imaging is still faced with the problem of high time complexity and multiple image reconstruction calculation. For this purpose, we designed the time-sharing multi-scale elastography and its optimization algorithm.

Multi-scale time-sharing elastic imaging: multi-scale strain elastic imaging is realized by establishing vertical mapping between linear discrete and distributed multi-scale data set or elastic medium and time-sharing plane. The elastography scheme enables the discrete points in medical imaging tissues to be approximated along the boundaries of concentrated areas and multi-scale fusion directions. Then, the multi-scale elastic weights of each segment of medical imaging tissue were obtained by time-sharing calculation. This method requires multi-objective optimization of elastic weight when solving practical problems. Multi-objective optimization needs to meet the following constraints:

(1) the contact surface between time-sharing interface and elastic tissue remains smooth all the time, that is, time-sharing and elasticity will not offset each other.
(2) the jitter of elastic weight of medical imaging tissue will not cause the deformation of multi-scale data set. Even if the data set deforms, it can be weakened by time-sharing.
(3) the fusion error between medical imaging and multi-scale is so small that the elastic weight inside the medical imaging tissue can be neglected.

Based on the above basis and statement, the multi-objective optimization problem of multi-scale time-sharing elastography is to maximize the efficiency of elastography by using the least time stratification and the least times of dimensionality reduction. The formal description of the problem is shown in formula (7).

$$\underset{subject\ \ to}{MOOSS} \quad \{\min h(x), \min_{x \in X \subseteq \{0,1\}^n} k(x), \max \eta(x)\} \tag{7}$$

To solve the above problems, we present the multi-objective linear integer optimization algorithm, namely algorithm II.A.

Transfer learning algorithm for clinicopathological features of cervical cancer

According to the statistical and analytical results of the characteristics of cervical cancer cases in literature [22, [23] and [24], as shown in Table 1, we found that the modeling of cervical cancer characteristics has the following difficulties:

(1) there is a very direct relationship between the characteristics of cervical cancer cases and clinical stage, the probability of organ metastasis and tumor size, etc., but this relationship is difficult to be analyzed by random process modeling. Table 2 shows the characteristic errors obtained by adopting several common random distribution models. Analysis of Table 2 shows that these errors are all greater than the differentiation differences in Table 1, which is unacceptable.
(2) the metadata structure is relatively complex. If only the low-dimensional vector is used to represent the metadata, a lot of important cervical cancer feature information will be lost, resulting in a large error in the cervical cancer feature extraction mechanism.

Table 1 Statistical analysis of cervical cancer characteristics (%) [22–24]

statistics	χ^2	P	differentiated
Cases of stage I	11	0	<0.5
Cases of stage II	46	2	<0.9
Cases of stage III	45	9	<0.9
Cases of stage IV	45	9	<0.9
adenocarcinoma	12	5	<0.8
Squamous cell carcinomas	81	4	<0.09
menopause	7	0.03	<0.059
Tumor size	9	0	<0.039
Viscera metastasis	14	0	<0.05

(3) it is difficult to reduce dimension. This high-difficulty dimensionality reduction may increase the spatial complexity of dimensionality reduction gradually and generated data sets with high redundancy.

In order to solve the above problems, we design a cervical cancer characteristic model based on bi-objective optimization. The model can also adaptively adjust the dimensionality reduction threshold according to the various situations described in Table 1.

Starting from the statistical distribution of cervical cancer characteristics, the cervical cancer model must have aggregated characteristic variables to facilitate feature extraction and screening. Therefore, the high-dimensional data sample set is transformed into several independent one-dimensional input variables. The characteristic model of cervical cancer cases can be established from the following two ideas.

The first is to eliminate the random variables that have negative effects on the classification of cervical cancer cases. For example, in some pathological classification, the random variables that inhibit the sensitivity to the classification of features should be removed. This matrix elimination method of random variables can be completed by referring to formula (8).

Table 2 Statistical errors of random distribution of cervical cancer characteristics(%)

Random distribution	error	Whether it can be tolerated
Bernoulli distribution	1.24	NO
Poisson distribution	2.09	NO
Binomial hair you do not	2.65	NO
Normal distribution	1.98	NO
Chi-square distribution	0.98	NO
An index distribution	>3.4	NO
Gamma distribution	<0.7	Maybe
Beta distribution	>2.76	NO

$$\begin{bmatrix} x_1 \\ x_2 \\ \vdots \\ x_{|P|} \end{bmatrix} \rightarrow \begin{bmatrix} x_1 \\ x_2' \\ \vdots \\ x_{|P|}' \end{bmatrix} \cdot \begin{bmatrix} y_1 \\ y_2 \\ \vdots \\ y_{|P|} \end{bmatrix}^T \rightarrow \begin{bmatrix} 1 \\ 0 \\ \vdots \\ 1 \end{bmatrix} \tag{8}$$

The matrix elimination method can convert random variables into integer variables for scheduling problems.

Therefore, the core of this model construction scheme is to transform the feature distribution of $|P|$ input random variables into $|P|$ single target one-dimensional random variable, as shown in Fig. 5.

The second model building scheme is based on an efficient and accurate dimensionality reduction strategy to find $|P|$ high-dimensional input variable to a low-dimensional feature space metadata transformation sequence. This sequence is called the cross-dimensional transformation vector of cervical cancer pathological features, as shown in Fig. 6. This transformation vector may be a linear or nonlinear matroid transformation of the original eigenvector, or an optimization vector with or without constraints, as shown in formula (9). Under the constraints of rapidly decreasing finite element, the model can minimize the redundancy and error of cervical cancer pathology classification.

$$\begin{bmatrix} x_1 \\ x_2 \\ \vdots \\ x_{|P|} \end{bmatrix}^T \cdot Y_{|FS|\times|p|} \rightarrow \begin{bmatrix} 1 \\ 0 \\ \vdots \\ 1 \end{bmatrix}^T \tag{9}$$

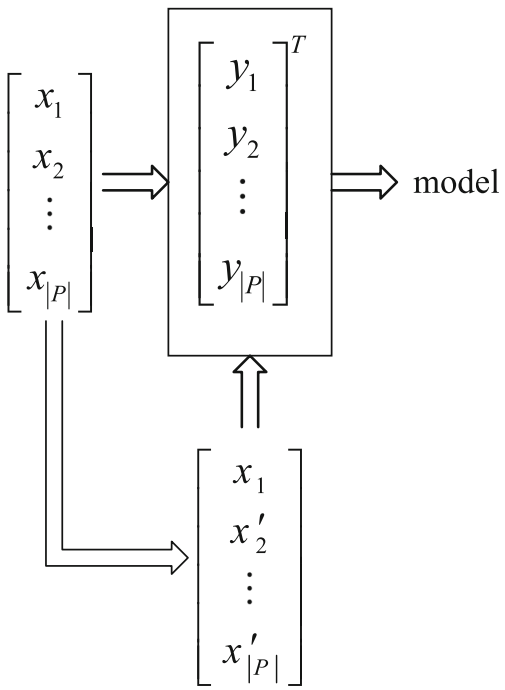

Fig. 5 The process of model establishment for removing characteristic matrix of cervical cancer

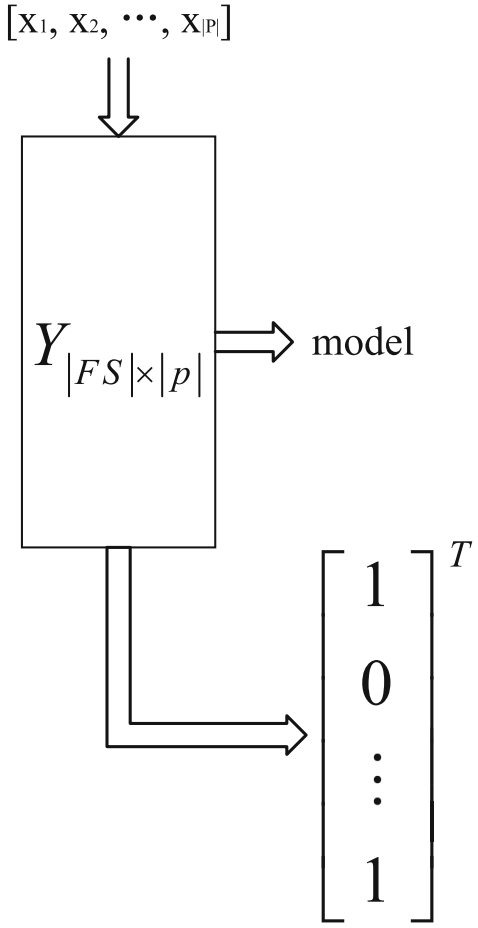

Fig. 6 Modeling process of metadata optimization based on finite element constraints

In order to realize the migration of pathological features of cervical cancer, we analyzed the constraints of the migration of pathological features, such as formula (10) and the limitation description (definition III.A).

$$\begin{cases} d_N \geq \sigma m_N \\ Q(x_i, \alpha) \geq \dfrac{|P|}{|FS|} \sum\limits_{j=1}^{|Y_i|} t_{ij} Q'(x_{i-1}, \sin\alpha) \\ t_{ij} \geq 0, \forall i, j \end{cases} \tag{10}$$

Where, d_N represents the network depth, m_N represents the feature dimension, and the function represents the metadata of data set x_i of i-th dimension after dimension reduction. The function is directly dependent on historical data.

Definition III. A the relationship between the time complexity of cervical cancer pathological feature model and the expectation and variance of random distribution is nonlinear.

In order to eliminate the above limitations, migration sensitivity and corresponding generalization ability were designed for different levels of characteristics of cervical cancer pathological feature transfer learning network. Among them, the bottom layer of the migration learning model evolves the type and scale of input variables into the migration sensitivity. In the application of migration learning in cervical cancer pathological feature extraction and screening, a linear mapping relationship was established between multi-source tasks and the training data set of migration learning network, and the redundancy of feature space caused by cross-dimensional supervised learning was also considered. The combination of metadata reconstruction and cross-dimensional migration is bound to weaken the marginal features of cervical cancer pathological feature model and strengthen the supervision effect, so the migration effect will be very good. Correspondingly, the metadata of marginal features in the upper layer of the migration learning network can be combined with the bottom training sample set that has been migrated to construct a cross-layer fusion and highly consistent cervical cancer pathological feature space and feature extraction reference frame. This reference system includes the basic unit of characteristic space and training data set of cervical cancer pathology recognition, which is beneficial for the subsequent migration and learning of the feature abstraction of the network layer.

We choose four different CNN structures of AlexNet [25], VGGM [26], VGG16 [27] and VGG19 [28], VGGM, VGG16 and VGG19. All four networks contain a convolutional layer and a full connection layer. Among them, the middle part of different network layers is defined as convolution layer, which is convenient for feature extraction. In addition, the upper layer of the migration network is the full connection layer, including the convolutional layer feature and the mapping interface of the full connection layer feature.

The network definition and processing of the transfer learning of clinical and pathological characteristics of cervical cancer are described as follows, and the algorithm description is detailed in algorithm III. A and III. B.

- **Step 1**: pre-train the pathological feature set of cervical cancer based on the model established in Figs. 5 or 6.

Subsets of the data set shown in Table 1 were used for the data set of pre-training cervical cancer pathological feature set. This subset contains 2020 cervical cancer CT images, approximately 1.5 million classified training pathological images, 34,500 pathological data and 80,000 clinical text cases.

- **Step 2**: extract the migration characteristics of high-quality metadata and reduced dimensional matrix.

Firstly, the pre-trained cervical cancer pathological feature set parameters were transferred to the dimensionality reduction matrix M and the monitoring matrix K, respectively. In order to ensure the credibility of cervical cancer pathological feature extraction, the feasible domain of cervical cancer symptom data set needs to be adjusted to the default input feasible domain required for pre-training cervical cancer

pathological feature set. Next, a linear mapping is established between the input and output values of the convolution layer and the full connection layer of the learning network. The output values of these levels correspond to the input values of the lower-dimensional vectors.

- **Step 3**: Normalize the characteristics of cervical cancer pathological feature set and supervised metadata matrix. The purpose of feature vector normalization is to make the cross-dimensional feature components of feature vectors have similar measurements at different levels of the learning network. The normalization process adopts L2 norm normalization method. Cervical cancer pathological feature set is regarded as a matrix. $\{I_1, I_{2,} ..., I_i, ..., I_m\}$ denotes the pathological characteristics of m cervical cancer in the data set, the normalization of a certain l-dimensional characteristic vector $j_i$and its L2 norm of pathological characteristics I_i of cervical cancer in the data set j_i^* is obtained:

$$\begin{cases} j_i = \left[x_i j_i^1, x_i j_i^2, ..., x_i j_i^k, ..., x_i j_i^{|P|}\right]^T \\ j_i^* = \dfrac{j_i}{\sqrt{\left(x_i j_i^1\right)^2 + \cdots + \left(x_i j_i^k\right)^2 + \cdots + \left(x_i j_i^{|P|}\right)^2}} \end{cases} \quad (11)$$

- **Step 4**: Repeat step 2 until the migration sensitivity is less than the threshold.
- **Step 5**: Repeat step 3 until the training is satisfactory.
- **Step 6**: return the pathological characteristic sequence and model matrix of cervical cancer.

The above process is shown in Fig. 7.

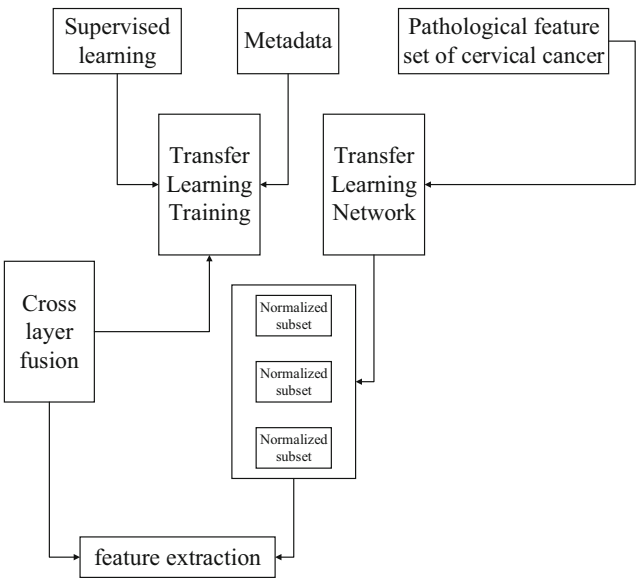

Fig. 7 Transfer learning process of clinical and pathological characteristics of cervical cancer

Medical intelligent computing system for clinical pathology of cervical cancer

In order to improve the accuracy and real-time of cervical cancer pathological analysis and clinical diagnosis, we designed a medical intelligent computing system suitable for cervical cancer clinical pathology. The system not only integrates the multi-scale time-sharing elastic imaging algorithm and the transfer learning algorithm of clinical and pathological characteristics of cervical cancer proposed above, but also has the following functions:

(1) the computational system can fully understand and learn the complex pathological information of cervical cancer through the simulation of pathological feature samples, the extension of cross-dimensional features and the expansion of metadata sets.
(2) the computing system can make multi-dimensional decisions and in-depth analysis, and apply migration learning to the multi-agent entity of anthropomorphic intelligence.
(3) the computing system can identify cervical cancer pathological objects and multi-dimensional pathological events. At the same time, the system can store abundant available pathological knowledge and has the ability of transfer learning reasoning and multi-dimensional prediction.
(4) the system can adapt to the complex learning environment and clinical feature extraction environment, and can obtain the pathological information to be concerned or recognized in real time and make appropriate feedback behavior.

The abstract general model of the medical intelligent computing system applicable to cervical cancer is shown in Fig. 8. In the process of solving the complicated clinical problems of cervical cancer, the system has the basic theory of pathological mechanism, support technology of feature transfer learning and cross-

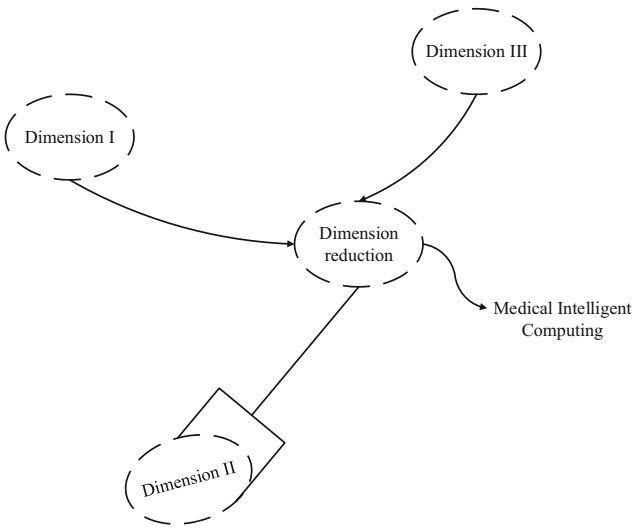

Fig. 8 Abstract general model of medical intelligent computing system

dimensional application. This system can not only overcome the defects of single dimension technology, but also eliminate the high redundancy of cervical cancer pathological feature analysis and the non-intelligent factors brought by dimension reduction by adopting different migration modes. The system can obtain the cross-dimensional expression ability of pathological knowledge and the self-adaptive reasoning ability driven by metadata from the transfer learning process. Therefore, the system can improve the efficiency of intelligent computing system and accelerate the speed of problem solving.

The main interfaces of the specific medical intelligent computing system in Fig. 8 include (1) system scheduling interface: the scheduling interface of the input/output data between the cervical cancer clinical environment and the intelligent computing system; (2) multi-scale time-sharing elastic imaging and feature computing interface: the interface between the intelligent computing system and the external environment through the multi-scale and cross-dimensional input/output system; (3) feature extraction and migration learning processing interface: real-time processing of the input and output data of (1) and (2), and optimizing the output.

To sum up, the medical intelligent computing system can be formally expressed as a seven-tuple:

$$\begin{cases} M_C = \{P, T^i{}_C, X, (T^i{}_L, T_X, P_a) | i = 1, 2, ..., |P|\} \\ P{:=}SS\ with\quad algorithm\ III.A \\ T^i{}_C{:=}i{-}th\ computing\quad iteration \\ X{:=}random\quad variable \\ T^i{}_L{:=}i{-}th\ transfer\quad learning \\ T_X{:=}random\quad distribution \\ P_a{:=}intelligent\quad computing\ set \end{cases} \tag{12}$$

According to the intelligent computing system defined by formula (12), the following properties can be obtained.

- **Property 1** for the intelligent computing system MC, t P_a is non-empty.
- **Property 2** the absolute value of the difference of the vector rank between P and P_a can reflect the complexity and intelligence of the intelligent computing system.
- **Property 3** The utility of MC in solving problem P U(P, P_a)∈[0, 1]. If U(P, P_a) = 1, it means that the medical intelligent computing system can completely solve the problem P. If U(P, P_a) = 0, the medical intelligent computing system is completely unable to solve the problem P. If 0 < U(P, P_a) < 1, the medical intelligent computing system can partially solve the problem P.
- **Property 4** a pathological feature of cervical cancer set is denoted by $I = \{i_1, i_2, ..., i_j, ..., i_{|P|}\}$. The cross-dimensional weight of feature set I is denoted by $W = \{w_1, w_2, ..., w_j, ..., w_{|P|}\}$. Any subset of pathological features is denoted by $\overline{I} = \left\{\bar{i}_k, \bar{i}_{k+1}, ..., \bar{i}_{k+u}, ..., \bar{i}_{\frac{|P|}{u}}\right\}$. Subset$\overline{I}$ is an intelligent computational feasible solution of pathological feature set I.

Meanwhile, the expected number of iterations of the subset $\overline{I}$ is calculated $E(\overline{I}) = \frac{|P|\sqrt{|M_C|}}{k+u} \sum_{v=1}^{\frac{|P|}{u}} \bar{i}_v$.

In addition, the rule codes of the above types of system interfaces are described as follows:

(1) system call class
class Invoking
{
int P(id)
public: f(int Pid)
{…}
virtual void
$M_{(|P|,|FS|)}$
}
(2) input and output classes
class IO
{
int id; I(id)
$T^i{}_C$
private:
First interface
X(id)
Modeling
Invoking interface
Mapping id
{…}
updating random variable X(id)
T_X
}
(3) transfer learning training function and feature extraction function:
class TL
$T^i{}_L$
instantiation of class Invoking
instantiation of class IO
public implementation:
subset $\overline{I}$ Implementation
{…}
Intelligent scheduling
{…}
computing Pa
{…}
}

Figure 9 shows the metadata-driven adaptive reasoning progress of the intelligent medical computing system. Here, the matching module is helpful to improve reasoning efficiency. The interfaces given in the above codes are directly connected with adaptive reasoning modules. The training set of transfer learning serves as the starting point of reasoning progress. The expectation of a subset ACTS as a corrective factor for reasoning. P_a serves as a reference frame for adaptive scheduling. The data flow of the adaptive inference is shown in Fig. 10.

System performance verification

The main contributions of this paper are the multi-scale time-sharing elastic imaging algorithm, the design of cervical cancer clinicopathological features transfer learning algorithm and the establishment of cervical cancer clinicopathological intelligent computing system. In order to verify the performance of the above algorithm and system, cervical cancer pathological samples were taken as input and Matlab simulated medical ultrasound transmission/receiving imaging system. C# realizes the medical intelligent computing system and takes Matlab output as input. In order to simplify the simulation model, we only consider the classification of experimental objects described in Table 3. Other parameters of the experimental environment are shown in Table 4.

For example, the accuracy of cervical cancer pathological feature extraction (Fig. 11), the elasticity scoring error of cervical cancer (Fig. 12), the lesion recognition rate (Fig. 13), and the system execution efficiency (Fig. 14 a and b) were compared.

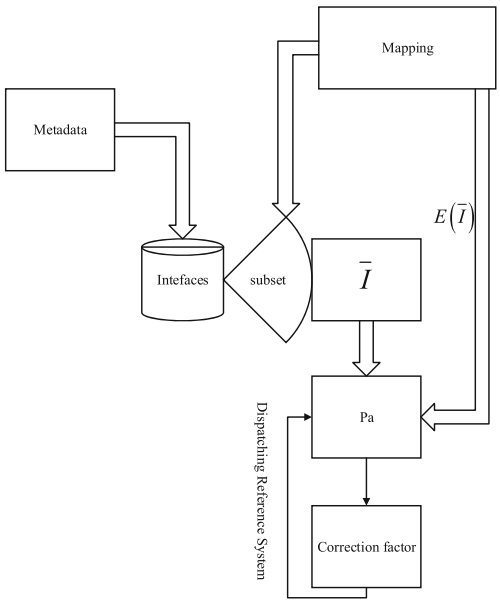

Fig. 9 Adaptive inference flow

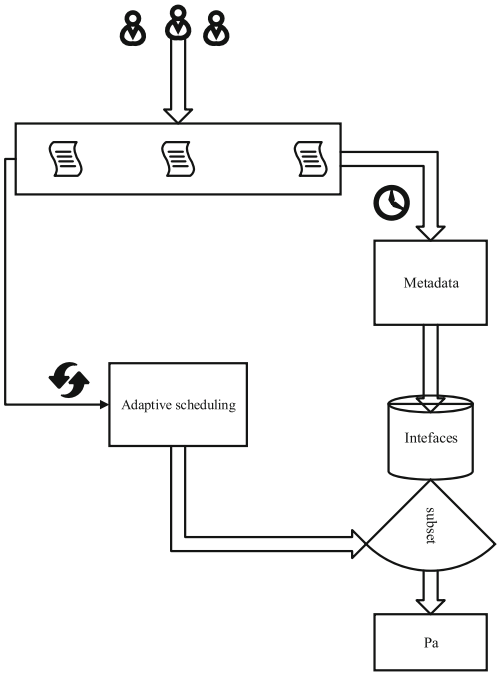

Fig. 10 Adaptive inferential data flow

Based on the above performance parameters, the following three algorithms are respectively compared and analyzed with single-scale Retinex (SSR). The migration learning (SSR-TL) based on single-scale Retinex and the proposed algorithm METS are described.

Figure 11 shows the single-scale Retinex (SSR) of the three algorithms. Based on the single-scale Retinex, migration learning (SSR-TL) and the proposed algorithm METS are shown in the accuracy of cervical cancer pathological feature extraction. With the increase of object classification, the accuracy of SSR-TL decreased significantly. This is because the increase in the classification of experimental objects makes the accuracy of single-scale image feature analysis not guaranteed. At the same time, SSR-TL performance also began to decline, but better than SSR performance. This is because transfer learning can make up for the deficiency of single scale. However, both SSR-TL and SSR performed poorly when the number of subjects was larger than 3. On the contrary, METS 'advantage in multi-scale and transfer learning is fully demonstrated. The scale of finite element data and low dimensional multiscale are related to high dimensional multiscale. The smaller the scale separation, the smaller the

Table 3 classification of subjects

statistics	χ^2	P
The cases I/II/III/IV	21	5
adenocarcinoma	8.6	3.5
Squamous cell carcinomas	41	3.4
Tumor size	11	0.5
Viscera metastasis	12	0.5

Table 4 Experimental settings

parameter	Value
The central frequency of the medical probe	8 MHz
Imaging of bandwidth	2.5 MHz
Image sweep band width	5 MHz
Number of ultrasound images of cervical cancer	245
Manually mark the image scale	35%
Real-time new image proportion	[5, 15]%
Proportion of malignant tumors	[1, 5]%
Proportion of benign tumors	[1, 5]%

scale of finite element data, and the faster the iterative convergence of low-dimensional multi-scale imaging. The larger the scale separation, the larger the scale of finite element data, and the faster the iterative convergence of high-dimensional multi-scale imaging.

Figure 12 describes the three algorithms of single-scale Retinex (SSR). Based on the single-scale Retinex, migration learning (SSR-TL) and the proposed algorithm METS 'performance in the elasticity score error of cervical cancer. This parameter can be used to evaluate the performance of the algorithm. This performance has a direct impact on the performance efficiency and spatial complexity of medical intelligent computing systems. With the increase of the classification of experimental objects, the requirements of multi-scale analysis and cross-dimension analysis are higher and higher. It is difficult for the single-scale algorithm to meet the expectation $E(\bar{I}) = \frac{|P|\sqrt{|M_C|}}{k+u} \sum_{v=1}^{\frac{|P|}{u}} \bar{i}_v$ of the number of iterations of the subset.

As can be seen from the expected expression, the single-scale algorithm is difficult to find a compromise point between k and u. As a result, the elastic score has a serious jitter,

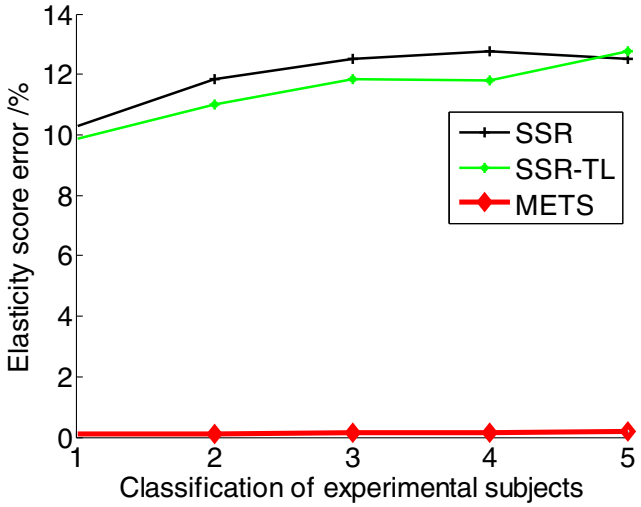

Fig. 12 Elasticity score error

resulting in a large error. When the classification of subjects was greater than 3, the errors of SSR and SSR-TL were 2 times higher than METS. The above performance improvement is attributed to the normalization of cervical cancer pathological feature set and features of supervised metadata matrix. The obtained eigenvectors are normalized so that the cross-dimensional eigen components of the eigenvectors have similar measurements at different levels of the migration learning network. The normalization process adopts L2 norm normalization method. Cervical cancer pathological feature set is regarded as a matrix.

Figure 11 shows three algorithms with a single scale Retinex (SSR). Based on the single scale Retinex, migration learning (SSR-TL) and the proposed algorithm METS 'performance in the recognition rate of lesions. As the classification of subjects increased, the recognition rates of SSR, SSR-TL and METS decreased. When the number of subjects was less than 3, the difference between the recognition rate of SSR-TL and METS was less than 3%. However, when the

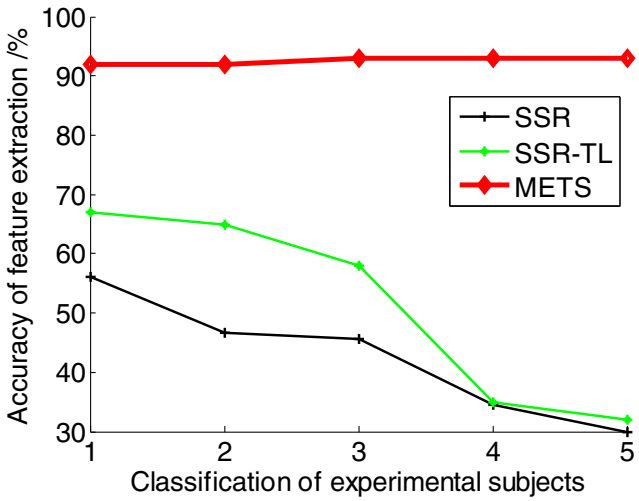

Fig. 11 Accuracy of feature extraction

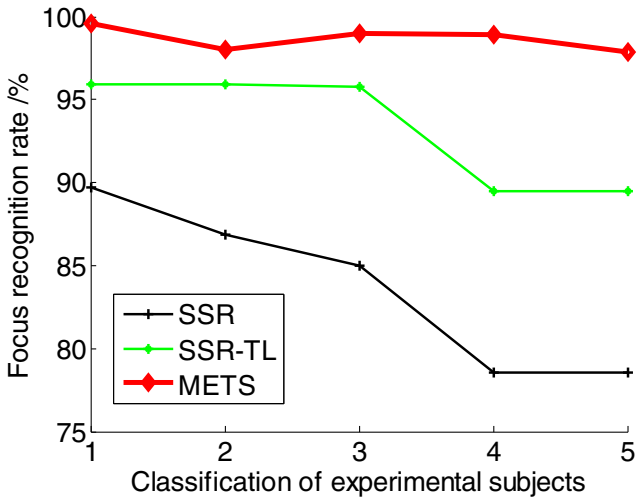

Fig. 13 Focus recognition rate

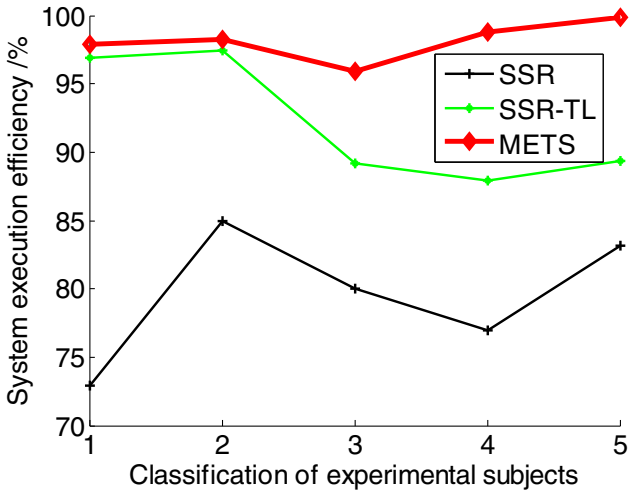

(a) Sample size

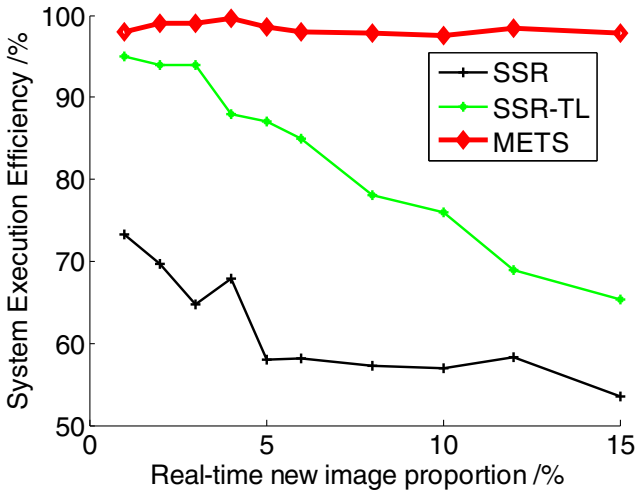

(b) Real-time new image proportion

Fig. 14 System Execution Efficiency

number of subjects was greater than 3, the disadvantages of SSR and SSR-TL were obvious. For SSR-TL, even if the accuracy of sample set is improved by migration learning, the recognition rate of lesions is very small. For the pathological characteristics of cervical cancer in the METS system, we designed the characteristics of different levels of the migration learning network and its migration sensitivity and corresponding generalization ability. Among them, the bottom layer of the migration learning model evolves the type and scale of input variables into the migration sensitivity. In the application of migration learning in cervical cancer pathological feature extraction and screening, a linear mapping relationship was established between multi-source tasks and the training data set of migration learning network, and the redundancy of feature space caused by cross-dimensional supervised learning was also considered. However, the migration learning of SSR-TL could not achieve the above effect, so the performance of SSR-TL would decline due to the complexity of experimental classification (Fig. 13).

Figure 14 describes three algorithms with a single scale Retinex (SSR). Based on the single scale Retinex, migration learning (SSR-TL) and the proposed algorithm METS 'performance in the execution efficiency of the medical computing system. We discuss the effects of sample size and the number of experimental objects on the performance of the system. As can be seen from Fig. 14 a, with the increase of sample size, the system execution efficiency of SSR first remained unchanged, and then decreased sharply. This is because the system is difficult to meet the requirements of feature modeling, extraction and imaging of large-scale samples. However, SSR-TL can better meet the above performance. But the gap with METS is growing. The difference ranges from about 5% at the top to about 1% at the bottom. The special feature is that as the proportion of real-time new images increases, the METS 'advantage is more obvious. The adaptive inference flow shown in Fig. 9 and the data flow shown in Fig. 10 can explain the basis of this advantage.

Conclusions

On the one hand, in order to reduce the data dimension and imaging error, this paper designs a multi-scale time-sharing elastic imaging algorithm. The algorithm can also reduce the time of high-resolution image reconstruction and meet the high requirement of data sample feature extraction. On the other hand, in order to eliminate the long queue of large-scale burst imaging tasks and the long establishment time of imaging data set, this paper proposed the transfer learning algorithm of clinical and pathological characteristics of cervical cancer based on the results of statistics and analysis of cervical cancer case characteristics and the difficulties in cervical cancer feature modeling. This paper established a medical intelligent computing system with high efficiency and reliability for the pathological analysis and calculation of cervical cancer. The system can optimize the time complexity of data dictionary imaging method and minimize the computational complexity of image reconstruction according to the multi-layer and multi-dimensional computing architecture. The experimental results show that the proposed algorithm performs well in such aspects as accuracy of cervical cancer pathological feature extraction, elasticity scoring error of cervical cancer, lesion recognition rate and system execution efficiency.

Compliance with ethical standards

Conflict of interest We declare that we have no conflict of interest.

Human and animal rights This article does not contain any studies with human participants or animals performed by any of the authors.

Informed consent Informed consent was obtained from all individual participants included in the study.

References

1. Waggoner, S. E., Cervical cancer. Lancet 361(9376):2217–2225, 2003.
2. Veronesi, U., Boyle, P., Goldhirsch, A. et al., Breast cancer. Lancet 365(9472):1727–1741, 2005.
3. Dougherty, T. J., Photosensitizers: therapy and detection of malignant tumors. Photochem. Photobiol. 45(S1):879–889, 2010.
4. Monticone, S., Burrello, J., Tizzani, D. et al., Prevalence and Clinical Manifestations of Primary Aldosteronism Encountered in Primary Care Practice. J. Am. Coll. Cardiol. 69(14):1811, 2017.
5. Raj, N., Valentino, E., Capanu, M. et al., Treatment Response and Outcomes of Grade 3 Pancreatic Neuroendocrine Neoplasms Based on Morphology: Well Differentiated Versus Poorly Differentiated. Pancreas 46(3):1, 2017.
6. Simon, I., Pound, C. R., Partin, A. W. et al., Automated image analysis system for detecting boundaries of live prostate cancer cells. Cytometry 31(4):287–294, 2015.
7. Yamaguchi, K., Nakazono, T., Egashira, R. et al., Diagnostic Performance of Diffusion Tensor Imaging with Readout-segmented Echo-planar Imaging for Invasive Breast Cancer: Correlation of ADC and FA with Pathological Prognostic Markers. Magnetic Resonance in Medical Sciences: MRMS An Official Journal of Japan Society of Magnetic Resonance in Medicine 16(3):245–252, 2017.
8. Zhang, X., and Yang, P. J., Imaging Algorithm for Multireceiver Synthetic Aperture Sonar. Electr. Eng. Technol. 14:471, 2019. https://doi.org/10.1007/s42835-018-00046-0
9. Bian, G., Yi, W., Bai, B. et al., Phased Array Imaging Algorithm for Endoscopic Ultrasound Based on Coded Excitation. Laser & Optoelectronics Progress 55(1):011103, 2018.
10. Zhang, G., Gao, W., Song, G. et al., An imaging algorithm for damage detection with dispersion compensation using piezoceramic induced lamb waves. Smart Mater. Struct. 26(2): 025017, 2017.
11. Becker, A. S., Perucho, J. A., Wurnig, M. C. et al., Assessment of Cervical Cancer with a Parameter-Free Intravoxel Incoherent Motion Imaging Algorithm. Korean J. Radiol. 18(3):510–518, 2017.
12. Wang, L. G., Li, L., Ding, J. et al., A Fast Patches-Based Imaging Algorithm for 3-D Multistatic Imaging. IEEE Geoscience & Remote Sensing Letters 14(6):941–945, 2017.
13. Shen H, George D, Huerta E. Glitch Classification and Clustering for LIGO with Deep Transfer Learning, 2017.
14. Peng, P., Tian, Y., Xiang, T. et al., Joint Semantic and Latent Attribute Modelling for Cross-Class Transfer Learning. IEEE Transactions on Pattern Analysis & Machine Intelligence 40(7): 1625–1638, 2017.
15. Ghazi, M. M., Yanikoglu, B., and Aptoula, E., Plant identification using deep neural networks via optimization of transfer learning parameters. Neurocomputing 235:228–235, 2017.
16. Ravishankar, H., Sudhakar, P., Venkataramani, R., et al., Understanding the Mechanisms of Deep Transfer Learning for Medical Images, 2017.
17. Fernandes, K., Cardoso, J. S., and Fernandes, J., Transfer Learning with Partial Observability Applied to Cervical Cancer Screening, 2017.
18. Pandey, B., and Mishra, R. B., Knowledge and intelligent computing system in medicine. Comput. Biol. Med. 39(3):215–230, 2009.
19. Sareen, S., Gupta, S. K., and Sood, S. K., An intelligent and secure system for predicting and preventing Zika virus outbreak using Fog computing. Enterprise Information Systems: 11(9):1–11(9)21, 2017.
20. Choi, Y. J., Baek, J. H., Park, H. S. et al., A computer-aided diagnosis system using artificial intelligence for the diagnosis and characterization of thyroid nodules on ultrasound: initial clinical assessment. Thyroid Official Journal of the American Thyroid Association 27(4):546, 2017.
21. Xia, K.-J., Yin, H.-S., and Zhang, Y.-d., Deep Semantic Segmentation of Kidney and Space-Occupying Lesion Area Based on SCNN and ResNet Models Combined with SIFT-Flow Algorithm. J. Med. Syst. 43(2), 2019. https://doi.org/10.1007/s10916-018-1116-1.
22. Xia, K. J., Yin, H. S., and Wang, J. Q., A novel improved deep convolutional neural network model for medical image fusion. Clust. Comput. 2018(3):1–13.
23. Kajian, X. I. A., Jiangqiang, W. A. N. G., and Yue, W. U., Robust Alzheimer Disease classification based on Feature Integration Fusion Model for Magnetic. Journal of Journal of Medical Imaging and Health Informatics 7:1–6, 2017.
24. Xiangfeng, L. U., Bingchen, H. U. A. N. G., and Fuxi, M. O., Comparative analysis of the clinicopathological characteristics of cervical cancer in young and middle-aged and elderly patients. China Medicine and Pharmacy. 9(3):25–28, 2019.
25. Qian, P., Xi, C., Min, X., Jiang, Y., Kuan-Hao, S., Wang, S., and Jr, R. F. M., SSC-EKE: semi-supervised classification with extensive knowledge exploitation. Inf. Sci. 422:51–76, 2018.
26. Qian, P., Sun, S., Jiang, Y., Kuan-Hao, S., Ni, T., Wang, S., and Jr, R. F. M., Cross-domain, soft-partition clustering with diversity measure and knowledge reference. Pattern Recogn. 50:155–177, 2016.
27. Qian, P., Zhou, J., Jiang, Y., Liang, F., Zhao, K., Wang, S., Su, K.-H., and Muzic, Jr., R. F., Multi-view maximum entropy clustering by jointly leveraging inter-view collaborations and intra-view-weighted attributes. IEEE Access 6:28594–28610, 2018.
28. Qian, P., Chung, F.-L., Wang, S., and Deng, Z., Fast graph-based relaxed clustering for large data sets using minimal enclosing ball. IEEE Trans. Syst. Man Cybern. B 42(3):672–687, 2012.